Structural and thermal confinement of Schwarz crystals

Dan Huang,[1,*] Huangliu Fu,[1,*] Meng Lyu,[2,*] Yuanwen Feng,[1] Ryoichi Kajimoto,[3] Mitsutaka Nakamura,[3] Takashi Honda,[4] Enke Liu,[2,†] Bing Li,[1,‡] Xiuyan Li,[1,5,§] and Ke Lu[1,5]

[1]*Shenyang National Laboratory for Materials Science, Institute of Metal Research, Chinese Academy of Sciences, Shenyang 110016, China*
[2]*Beijing National Laboratory for Condensed Matter Physics, Institute of Physics, Chinese Academy of Sciences, Beijing 100190, China*
[3]*Materials and Life Science Division, J-PARC Center, Japan Atomic Energy Agency, Tokai, Ibaraki 319-1195, Japan*
[4]*Institute of Materials Structure Science, High Energy Accelerator Research Organization (KEK), Tsukuba, Ibaraki 305-0801, Japan*
[5]*Liaoning Academy of Materials, Shenyang 110167, China*

(Received 22 October 2025; revised 23 April 2026; accepted 9 June 2026; published 6 July 2026)

As a nontrivial state of solid, Schwarz crystal manifests itself in extremely refined nanograins and triply periodic minimal surface (TPMS) grain boundaries, and therefore exceptional thermal and mechanical stability. However, it remains unexploited how the structural units interact and thermal transport is influenced by such complex atomic structures. Here, we investigate Schwarz crystals of Cu and Pt using neutron scattering and thermal transport measurements. Pair distribution function analysis reveals the coexistence of compressed grains and expanded TPMS grain-boundary regions, forming a spatially confined atomic environment. This leads to an unusual phonon hardening suggested by inelastic neutron scattering. As bulk materials, Schwarz crystals exhibit a quasilinear temperature dependence of thermal conductivity, which was previously only observed in low-dimensional materials. This contrast indicates that the spatial confinement of the Schwarz crystals plays a crucial role in determining the unique thermal conductivity, which also provides an emergent route to regulate thermal properties in bulk materials.

DOI: 10.1103/lqy2-cshl

I. INTRODUCTION

Solids are usually categorized into single crystal, polycrystal, quasicrystal, and amorphous solid, representing structural extremes from perfect atomic order to complete disorder. Recently, a nontrivial state of solid, named as Schwarz crystal, has emerged [1], characterizing an unprecedented atomic arrangement. The Schwarz crystal describes a metastable microstructure that emerges in face-centered-cubic metals such as Cu, Pt, and Al-Mg alloys when their grains are refined to only a few nanometers via cryogenic high-pressure torsion [2–4]. Its structural signature is the rearrangement of ordinary grain-boundary networks into triply periodic minimal surface (TPMS) grain boundaries, stabilized by a high density of coherent twin boundaries [5,6]. These TPMS grain boundaries exhibit topological structural features, which suppress grain growth even at temperatures close to the melting point and enable the combination of near-theoretical strength and exceptional thermal stability.

While the overall structural profile of Schwarz crystals has been revealed, the microscopic nature of the confined crystal remains poorly understood. In particular, it is still unclear how ordered nanograins and disordered grain-boundary networks arrange and interact at the atomic scale, and how confinement influences lattice vibrations. An important challenge is to unravel how the TPMS grain-boundary network modifies the local atomic environments, thereby giving rise to distinct physical properties. Resolving these questions is essential for clarifying the unique structure of Schwarz crystals and for establishing the geometric confinement distinguishes them from the common nanocrystalline. More importantly, it will extend our understanding of thermal conduction in complex metals by linking the spatial confinement of Schwarz crystals to the vibrational dynamics.

Given the distinctive microstructure of Schwarz crystals marked by disordered grain boundaries and spatially confined grains, profound effects on phonon-mediated thermal transport are anticipated. In disordered materials, phonon-mediated thermal transport behavior deviates significantly from the conventional $\kappa \propto T^3$ law, typically observed in crystalline solids at low temperatures [7,8]. Due to the absence of long-range order, the wavelike propagation of phonons is severely suppressed, resulting in heat being predominantly conducted through diffusive modes and localized vibrational states [9,10]. Several studies have shown that in such systems, thermal conductivity is extremely low and typically follows an approximate $\kappa \propto T^2$ behavior in the subKelvin regime [11–13]. On the other hand, when the material dimensions are reduced to the scale comparable to or smaller than the

*These authors contributed equally to this work.
†Contact author: ekliu@iphy.ac.cn
‡Contact author: bingli@imr.ac.cn
§Contact author: xyli@imr.ac.cn

dominant phonon wavelengths, spatial confinement effects induced by boundaries can significantly modify the phonon density of states (PDOS) and group velocity [14–16], thereby substantially affecting the thermal conductivity [17,18]. These investigations imply that the confined architecture of Schwarz crystals suppresses long-range phonon propagation, thereby playing a crucial role in modulating the material's thermal transport properties.

In this article, we investigate the atomic structure, lattice dynamics, and their impact on thermal transport of Schwarz crystals using neutron pair distribution function (PDF) analysis, inelastic neutron scattering (INS) measurement, and thermal transport measurements. These complementary results reveal structural confinement in Schwarz crystals, accompanied by broadened phonon spectra, phonon hardening, and a linear low-temperature thermal conductivity. We explicitly connect the structure of Schwarz crystals to their lattice dynamics and thermal transport. Schwarz crystals exhibit ultralow thermal conductivity with a quasilinear temperature dependence. In particular, Pt samples with smaller structural units show even a smaller power-law exponent in $\kappa(T) \propto T^{\alpha}$. For the first time, our findings identify a distinct thermal transport behavior associated with strong structural confinement and enhanced phonon scattering in Schwarz crystals.

II. EXPERIMENTAL METHODS

Coarse-grained, ultrafine-grained, and Schwarz Cu and Pt samples were prepared by recrystallization annealing, cryogenic plastic deformation, and high-pressure torsion (HPT), respectively. Disk-shaped specimens with a diameter of 5 mm were punched from sheets and processed by HPT at approximately 10 GPa and 30 rpm. The different microstructures were obtained by controlling the true strain. For Cu, coarse-grained samples were produced by annealing at 500 °C for 2 h, resulting in fully recrystallized grains with an average size of about 25 μm. Ultrafine-grained and Schwarz Cu samples corresponded to HPT true strains of $\varepsilon = 11$ and 72, respectively. For Pt, coarse-grained samples were annealed at 700 °C for 2 h, yielding recrystallized grains of about 140 μm. Ultrafine-grained and Schwarz Pt samples were prepared under the same strain conditions as Cu. The microstructures of Schwarz Cu and Pt were characterized by scanning electron microscopy and transmission electron microscopy (TEM). Specimens were prepared by cutting, mechanical grinding, and ion milling using a Leica RES101 and a Gatan 695 precision ion polishing system at liquid-nitrogen temperature.

The temperature-dependent thermal conductivity was measured using the thermal transport option of the Physical Property Measurement System (PPMS, Quantum Design) with an adiabatic one-heater, two-thermometer configuration. Due to geometrical uncertainties, the typical error in thermal conductivity measurements is estimated to be within ±10%. To generate a temperature gradient, a resistive heater was mounted on a gold-plated copper plate attached to one end of the sample. The thermal gradient was applied along the longest axis of the sample. A gold-plated copper plate connected to the puck clamp served as the heat sink. For temperature sensing, two gold-plated copper leads were attached directly to the sample using silver epoxy, aligned along the direction of the thermal gradient. Measurements were performed over a temperature range of 2–350 K.

The PDF experiments were conducted on the NOVA diffractometer at J-PARC [19]. The samples were sealed into a standard V-Ni cell with ^{3}He exchange gas. The empty container, the empty instrument, and a vanadium standard for normalization purposes were measured. A vanadium rod, an empty sample cell, and an instrumental background were also measured. The scattered neutrons ($0.12\,\text{Å} \leqslant \lambda \leqslant 8.3\,\text{Å}$) were detected with position-sensitive proportional counters installed at scattering angle 2θ of 72.7°–107.4°. The background contributions were measured at the same temperature and subtracted. The reduced pair distribution function, $G(r)$, was obtained by Fourier transforming the normalized structure factor $S(Q)$ using Python scripts developed by the NOVA team. The transformation from $S(Q)$ to $G(r)$ was carried out using the equation as follows:

$$G(r) = \frac{2}{\pi}\int_0^{\infty} Q[S(Q) - 1]\sin(Qr)\,\mathrm{d}Q, \tag{1}$$

where $Q = 4\pi \sin\theta/\lambda$ is the scattering vector.

The INS experiments were conducted on the 4SEASONS spectrometer at J-PARC [20]. In this study, an incident energy of $E_\mathrm{i} = 50$ meV was used, and the rotation speed of the Fermi chopper was set to 400 Hz to balance sufficient signal intensity with optimized energy resolution. The energy resolution of the instrument, given as the full width at half maximum, ranged from approximately $\Delta E = 0.4$ to 2.0 meV for energy transfers between 0 and 50 meV under an incident energy of $E_\mathrm{i} = 50$ meV. All samples were sealed in aluminum cans, and an empty can was measured under the same conditions for background subtraction. The scattering function $S(Q, E)$ was collected as a function of momentum transfer (Q) and energy transfer (E), with the momentum integration range set to $1\,\text{Å}^{-1} \leqslant Q \leqslant 8\,\text{Å}^{-1}$. The experimental data were preprocessed and analyzed using the *Utsusemi* software [21], and then converted into the generalized PDOS, g(E), using the following equation:

$$g(E) = \int \frac{E}{Q^2} S(Q, E)(1 - e^{-E/k_\mathrm{B}T})\,\mathrm{d}Q, \tag{2}$$

where k_B is Boltzmann's constant and T is temperature.

III. RESULTS AND DISCUSSION

Figures 1(a) and 1(b) show high-resolution TEM images of the Schwarz crystal samples of Cu and Pt, respectively. The grain size and corresponding microstructural characterizations of the samples are also included in Figs. S1 and S2 of the Supplemental Material [22]. Both samples exhibit highly interconnected grain-boundary network structures with average grain sizes of ∼3 nm for Cu and ∼2 nm for Pt. These TEM images provide structural evidence for the Schwarz samples, while the quantitative TPMS grain-boundary morphology has been established in our recent dark-field electron tomographic reconstruction work [23]. Together, these results distinguish Schwarz crystals from conventional nanocrystalline configurations.

PDF is a powerful technique for probing the local atomic structure of Schwarz crystals because it captures atomic

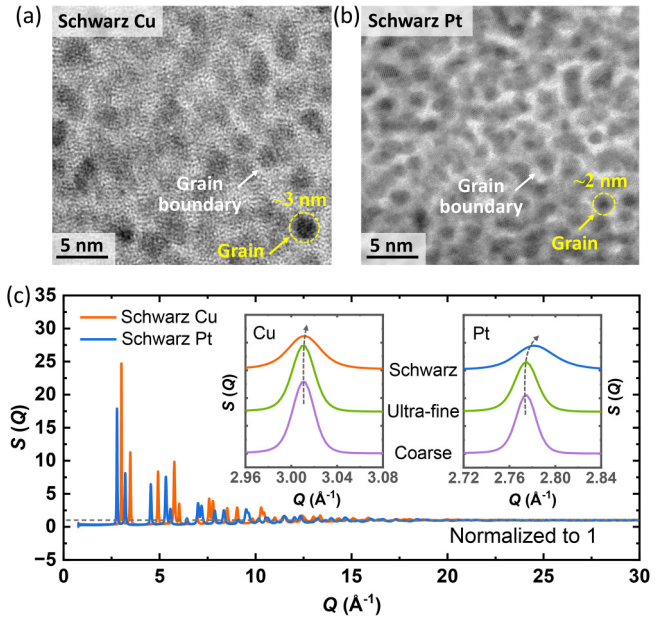

FIG. 1. (a), (b) High-resolution TEM images of Schwarz-structured Cu and Pt, showing nanoscale grain structures and well-defined grain boundaries. The average grain size is ∼3 nm for Cu and ∼2 nm for Pt. (c) Neutron scattering structure factor $S(Q)$ curves of Schwarz Cu and Pt. Insets display magnified views of the first diffraction peak for Cu and Pt. The dashed arrows indicate a rightward shift of the diffraction peaks in Schwarz crystals relative to coarse-grained and ultrafine-grained samples.

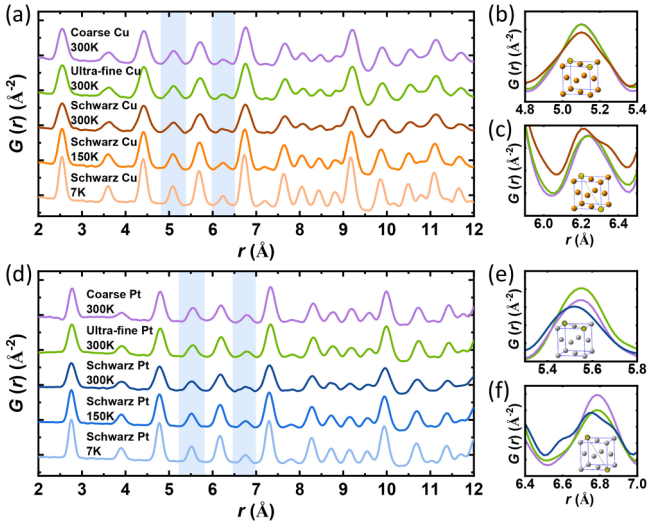

FIG. 2. (a), (d) $G(r)$ of Cu and Pt samples with different microstructures and temperatures. (b), (c), (e), and (f) Magnified views of specific peaks in panels (a) and (d), highlighting the splitting of PDF peaks at selected r regions. "Coarse," "Ultrafine," and "Schwarz" refer to coarse-grained, ultrafine-grained, and Schwarz samples, respectively. The Schwarz samples exhibit broader peaks, reduced intensities, and clear peak splitting, indicating a higher degree of structural disorder and the coexistence of diverse local atomic environments. The insets in panels (b), (c), (e), and (f) illustrate the atomic pairs corresponding to the enlarged PDF peaks.

correlations that are hidden in conventional crystallographic investigations [24]. Figure 1(c) shows the normalized neutron scattering structure factor $S(Q)$ curves of Schwarz crystal Cu and Pt samples up to 30 Å^{-1}, obtained from neutron total scattering. The corresponding $S(Q)$ curves for samples with different grain structures and temperature conditions are provided in Fig. S3 of the Supplemental Material [22]. It can be seen that the curves are well normalized to 1 at higher Q. In the low Q-range (2–10 Å^{-1}), both samples exhibit multiple sharp Bragg peaks, indicating that despite pronounced disorder, long-range periodicity is preserved. The inset further highlights that the peaks of the Schwarz samples are significantly broader than those of ultrafine-grained and coarse-grained references, consistent with smaller grain sizes. In addition, the first Bragg peak (111) of the Schwarz Cu and Pt samples shifts slightly to higher Q, corresponding to a compressed lattice state induced by strong internal stresses from curved grain boundaries and dense twin boundaries [2].

The normalized $S(Q)$ data were converted into PDF through Fourier transformation with a $Q_{\max}$ of 60 Å^{-1}. Figure 2 presents the PDF for Cu and Pt samples with different grain structures (coarse-grained, ultrafine-grained, and Schwarz structures) measured at 300, 150, and 7 K. Figures 2(a) and 2(d) show the full PDF curves for Cu and Pt, respectively. As seen in the figures, the coarse-grained and ultrafine-grained samples exhibit sharp, well-defined peaks at 300 K. In contrast, the PDF peaks of the Schwarz samples are noticeably broadened, with reduced intensities and significantly shortened coherence lengths (see Fig. S4 in the Supplemental Material [22]). These features indicate enhanced local structural disorder and strain in the Schwarz samples, reflecting their more diverse local atomic environments.

The blue shaded regions in the figure highlight the r ranges where the most significant structural deviations occur in the Cu and Pt samples, respectively. To more clearly reveal local structural features, Figs. 2(b) and 2(c) provide magnified views of two representative peaks in the PDF of the Cu samples, corresponding to interatomic distances along the face diagonal and body diagonal directions. Compared to the coarse-grained and ultrafine-grained samples, the Schwarz Cu sample exhibits pronounced peak splitting at these positions, indicating modifications of the local coordination environment. Figures 2(e) and 2(f) display the corresponding regions for the Pt samples, showing a similar trend to that observed in Cu. Notably, the peak splitting in the Schwarz crystal Pt is even more pronounced than that in the Schwarz crystal Cu, suggesting a higher degree of local structural distortion.

The peak splitting observed in the PDF of the Schwarz crystals results from the coexistence of three distinct local atomic environments: the conventional matrix phase, highly compressed grains, and TPMS grain boundaries. This feature can be understood as a consequence of strong spatial confinement imposed by the TPMS grain-boundary network, consistent with TEM observations and atomistic simulations [2,5]. It reflects a more complex local atomic structure relative to conventional coarse-grained, ultrafine-grained, and even nanocrystalline metals. In typical nanocrystalline materials, reduced grain size or increased microstrain mainly leads to continuous PDF peak broadening while preserving a single average interatomic distance [25]. In contrast, the Schwarz

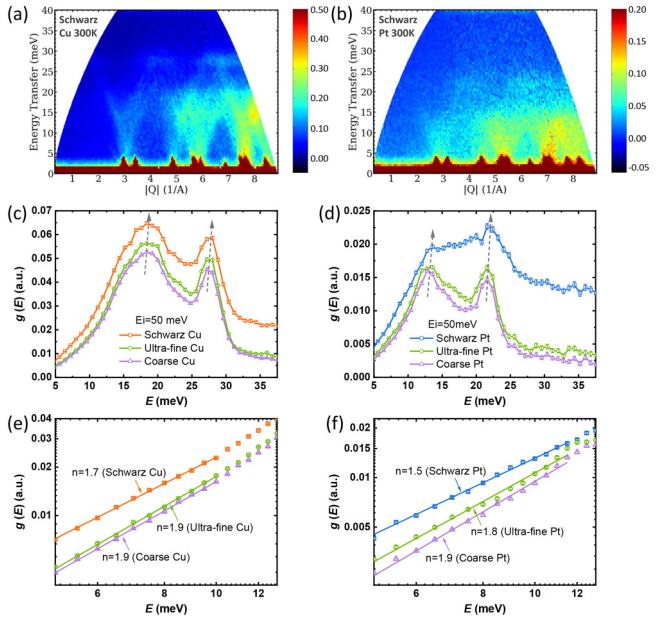

FIG. 3. INS data in Schwarz crystals, ultrafine, and coarse-grained Cu and Pt samples at 300 K. Contour plots of $S(Q, E)$ for (a) Cu and (b) Pt Schwarz samples as a function of momentum transfer Q and energy transfer E. PDOS extracted from INS data at incident energy $E_i = 50$ meV for (c) Cu and (d) Pt samples. The dashed arrows highlight the hardening of phonon modes in Schwarz crystals compared with ultrafine and coarse-grained references. (e), (f) Power-law fits of the low-frequency phonon density of states for Cu and Pt systems.

samples exhibit peak splitting across multiple coordination shells, indicating distinct local environments with different characteristic bond lengths. To our knowledge, this PDF work provides the first direct insight into the short-range atomic environments of grain boundaries in Schwarz crystals, which are inaccessible to conventional diffraction techniques.

INS enables direct probing of lattice dynamics [26–32]. We conducted INS experiments on samples with different microstructures, including coarse-grained, ultrafine-grained, and Schwarz crystals. Figures 3(a) and 3(b) show the dynamic structure factor $S(Q, E)$ for Schwarz-structured Cu and Pt. Compared to the coarse-grained and ultrafine-grained samples (see Fig. S5 in the Supplemental Material [22]), the dispersion of the Schwarz samples is significantly broadened and exhibits typical lattice stiffening behavior at low temperatures (see Fig. S6 in the Supplemental Material [22]). We further calculated the PDOS for various Cu and Pt samples from $S(Q, E)$, as shown in Figs. 3(c) and 3(d). The PDOS profiles of the coarse-grained and ultrafine-grained samples are consistent with previously reported results for coarse-grained Pt and nanocrystalline Cu [33,34]. In contrast, the Schwarz crystals exhibit pronounced peak broadening of phonon modes, attributed to the extensive structural disorder in the grain-boundary regions, as revealed by the TEM images in Fig. 1. More importantly, Schwarz crystals show noticeable hardening of modes and such hardening is more remarkable for the Schwarz Pt sample, as indicated by the dashed arrows in Figs. 3(c) and 3(d). The behavior originates from lattice compression induced by the internal stress state of the Schwarz structure, as evidenced by the rightward shift of the first peak of the $S(Q)$ curves from the neutron total scattering (Fig. 1) and the lattice hardening revealed by the dynamic structure factor $S(Q, E)$ from INS measurements (Fig. S5 in the Supplemental Material [22]). Such vibrational mode hardening not only reflects the intrinsic stress environment but also provides a microscopic basis for their unconventional phonon transport behavior.

In the low-frequency region, the PDOS of the Schwarz crystals is markedly different from that of the coarse-grained and ultrafine-grained counterparts. We performed power-law fitting of the low-frequency region of the PDOS curves, as shown in Figs. 3(e) and 3(f), focusing on the relation $g(E) \sim E^n$ to evaluate deviations from the ideal three-dimensional Debye model, where the exponent of $n = 2$ [35,36]. For the coarse-grained and ultrafine-grained Cu and Pt samples, the extracted exponents are close to 2, consistent with Debye-like behavior. However, the exponent n of the Schwarz crystals is notably reduced, $n = 1.7$ for Cu and $n = 1.5$ for Pt. Such reduced exponents are not unique to Schwarz crystals. Similar values in the range of $1 < n < 2$ have been reported in nanocrystalline and other structurally disordered systems (Table S1 in the Supplemental Material [22]), where grain-boundary-related disorder or the lack of long-range order leads to non-Debye vibrational behavior [16,36–38].

To investigate the influence of the unique structures on thermal transport, we measured the thermal conductivities of Schwarz, ultrafine-grained, and coarse-grained Cu and Pt [Fig. 4(a)]. In the low-temperature regime, Schwarz Cu and Pt exhibit strongly suppressed lattice thermal conductivity relative to their coarse-grained and ultrafine-grained counterparts. With increasing temperature, κ rises gradually and deviates from the low-temperature trend above ~65 K, consistent with the onset of stronger phonon-phonon scattering. The lattice contribution was estimated by subtracting the electronic contribution from the measured total thermal conductivity using the Wiedemann-Franz relation [39]:

$$\kappa_{\text{lattice}} = \kappa_{\text{total}} - \frac{L_0 T}{\rho(T)}, \tag{3}$$

where $\rho(T)$ is the measured electrical resistivity and $L_0 = 2.44 \times 10^{-8}\,\text{W}\,\Omega\,\text{K}^{-2}$. The detailed calculation procedure and electrical resistivity data are provided in the Supplemental Material and Fig. S7 [22]. As shown in Fig. 4(b), Schwarz Cu sample 1 follows $\kappa \propto T^{1.26}$, sample 2 follows $\kappa \propto T$, and Schwarz Pt follows $\kappa \propto T^{0.87}$. The difference between Cu samples 1 and 2 is consistent with their distinct characteristic grain sizes in Fig. S1 of the Supplemental Material [22].

In this study, Schwarz crystals of Cu and Pt exhibit anomalously low thermal conductivity, with $\kappa(T)$ showing an almost linear temperature dependence over a broad low-temperature range. This behavior is clearly distinct from the T^3 dependence expected in ideal crystals and the T^2 law typically associated with amorphous solids [7,8,12,40]. Such anomalous lattice thermal transport resembles the phonon transport regime discussed for low-dimensional materials, in which long-wavelength phonons contribute less effectively to heat conduction, while heat is carried predominantly through random hopping and localized vibrational modes [41,42].

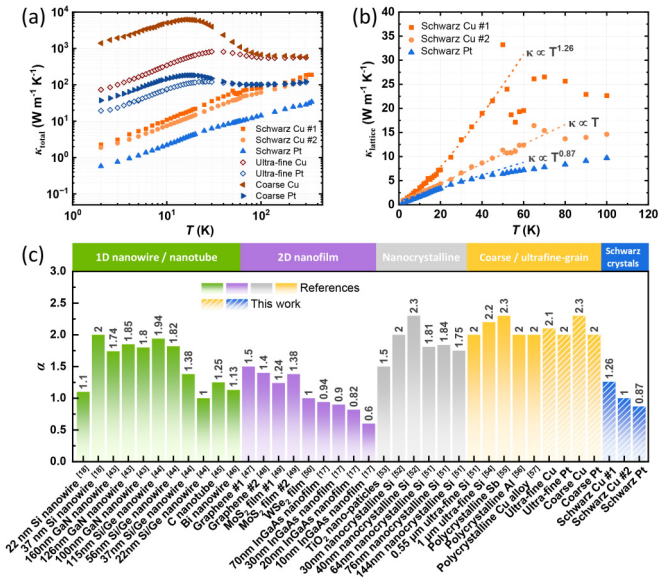

FIG. 4. Lattice thermal conductivity in Schwarz crystals and comparison with various materials. (a) Logarithmic plot of the total thermal conductivity, κ_{total}, as a function of temperature for Schwarz-structured Cu and Pt, together with ultrafine-grained and coarse-grained Cu and Pt. (b) Low-temperature κ_{lattice} of Schwarz crystals, showing a power-law behavior, with $\kappa \propto T^{1.26}$ for Schwarz Cu sample 1, $\kappa \propto T$ for Schwarz Cu sample 2, and $\kappa \propto T^{0.87}$ for Schwarz Pt. (c) Comparison of the power-law exponent α for Schwarz crystals with various low-dimensional materials [17,18,43–50], nanocrystalline materials [51–53], and coarse-grained and ultrafine-grained materials [51,54–57]. The hatched bars indicate the present work.

To elucidate the nearly linear thermal transport behavior, the lattice thermal conductivity of Schwarz crystals is compared with that of various material systems, including nanowires/nanotubes [18,43–46], thin films [17,47–50], and nanocrystalline materials [51–53], as shown in Fig. S8 of the Supplemental Material [22]. The results indicate that many low-dimensional materials also exhibit a power-law temperature dependence with exponents $\alpha < 2$ in $\kappa_{\text{lattice}} \propto T^{\alpha}$, which is characteristic of strongly scattered phonon transport. Figure 4(c) summarizes the power-law exponents α for the different samples. The α values of the Schwarz Cu and Pt samples are both close to 1, resembling the behavior observed in one-dimensional nanowires with small cross sections and two-dimensional materials with reduced thickness. Notably, these exponents are substantially smaller than 3 for ideal phonon boundary scattering [7,8], and also lower than $2-3$ for the ultrafine-grained and coarse-grained samples [Fig. 4(c) and Fig. S7 in the Supplemental Material [22]; see also Table S2 in the Supplemental Material [22]]. These comparisons further demonstrate the unusual thermal transport nature of the Schwarz crystals.

Schwarz crystals possess a periodic TPMS grain-boundary network structure, where thermal transport pathways are strongly confined with characteristic scales approaching or below the phonon mean free path. This spatial confinement suppresses phonon propagation, leading to behaviors that phenomenologically resemble those of low-dimensional systems, exhibiting an approximately linear temperature dependence at low temperatures [16,58,59]. For clarity, a comparison of low-temperature thermal conductivity exponents and corresponding mechanisms in representative material systems is now included as Table S2 in the Supplemental Material. Although such a quasilinear $\kappa \propto T$ behavior has been reported in low-dimensional materials, it is highly unusual in bulk materials. Schwarz crystals, however, remain pure metallic bulk materials. As summarized in Table S2 of the Supplemental Material [22], typical bulk systems, including single crystals, polycrystals, nanocrystalline bulks, and glasses, generally exhibit low-temperature exponents in the range of $2-3$. In contrast, Schwarz crystals are characterized by a continuously TPMS grain-boundary network that imposes isotropic spatial confinement on the grains. This unique structure not only gives rise to the observed quasilinear $\kappa \propto T$ behavior, but is also accompanied by a broadened PDOS with some features shifted toward higher energies, indicative of phonon hardening. This behavior is therefore distinct from the phonon softening more commonly reported in nanocrystalline and amorphous materials [16,60–62]. These results suggest that the unusual phonon transport observed in a pure metallic bulk system is associated with spatial confinement imposed by the unique Schwarz structure.

Both Schwarz Cu and Pt crystals exhibit unusual phonon hardening and an approximately linear temperature dependence of thermal conductivity at low temperatures, whereas Pt shows lower thermal conductivity and a smaller power-law exponent α. TEM and PDF analyses reveal that Schwarz Pt contains smaller structural units and a more confined atomic environment. Moreover, the PDOS of Schwarz Pt exhibits a gentler low-frequency behavior and a more pronounced high-frequency tail, indicating a stronger deviation from Debye-like behavior [35,36] and enhanced phonon scattering, respectively [16]. Consequently, Pt exhibits stronger anharmonicity and weaker thermal transport compared to Cu. For sample 2 of Cu contains a higher fraction of Schwarz structure than sample 1, consistent with previous reports that greater hardness correlates with smaller grain size and increased Schwarz content [1,6]. As a result, Cu sample 2 shows lower thermal conductivity and a smaller exponent α. These results suggest that increasing the fraction of Schwarz structure, characterized by densely curved grain boundaries, leads to more tortuous phonon transport paths, shorter mean free paths, and suppressed thermal conductivity. Notably, although phonon hardening observed in INS measurements generally enhances thermal conductivity in conventional crystals, Schwarz crystals, however, display drastically reduced lattice thermal conductivity due to confinement effects. These findings establish confinement-controlled phonon localization as an additional thermal transport mechanism in metals, complementing the conventional crystalline $\kappa \propto T^3$ and amorphous $\kappa \propto T^2$ models [7,8,11–13].

IV. CONCLUSIONS

In conclusion, we combined high-resolution TEM, PDF, INS, and low-temperature thermal conductivity measurements to investigate the structure and thermal transport of Cu and Pt Schwarz crystals. These multiscale observations demonstrate

that Schwarz crystals constitute a structural state distinct from conventional crystals, in which strong spatial confinement by TPMS grain boundaries alters lattice dynamics, leading to phonon hardening and quasilinear $\kappa(T)$ behavior at low temperatures. Pt samples further display lower thermal conductivity than Cu, attributable to their smaller grain size and stronger spatial confinement. Overall, these results reveal an unusual low-temperature phonon transport behavior in bulk metals governed by structural confinement and provide a clear pathway for tailoring thermal conductivity via grain-boundary control.

ACKNOWLEDGMENTS

This work was financially supported by the Strategic Priority Research Program of the Chinese Academy of Sciences (Grant No. XDB0510302), the National Natural Science Foundation of China (Grants No. 52225102, No. 52425107, and No. 52501264), the China Postdoctoral Science Foundation (Grant No. 2024M763337), and the Natural Science Foundation of Liaoning province (Grant No. 2024-BSBA-43). The authors acknowledge beam time awarded by J-PARC (Proposals No. 2024A0162 and No. 2024A0181). The authors thank Xueting Zhao, Haoyu Wang, and Chen Liang for their assistance with the sample preparation and neutron experiments. The authors also gratefully acknowledge Dr. Dehong Yu for the insightful discussions.

DATA AVAILABILITY

There are no publicly available research data or software supporting this manuscript. Requests for further information or data should be sent to the authors.

[1] K. Lu, A novel metastable structure in polycrystalline metals with extremely fine grains: Schwarz crystal, Metall. Mater. Trans. A **55**, 1 (2024).

[2] X. Y. Li, Z. H. Jin, X. Zhou, and K. Lu, Constrained minimal-interface structures in polycrystalline copper with extremely fine grains, Science **370**, 831 (2020).

[3] W. Xu, B. Zhang, X. Y. Li, and K. Lu, Suppressing atomic diffusion with the Schwarz crystal structure in supersaturated Al–Mg alloys, Science **373**, 683 (2021).

[4] H. Fu, X. Zhou, Z. Gao, Z. Jin, X. Li, and K. Lu, Effect of grain geometry on the stability of polycrystalline Pt at the nanoscale, Phys. Rev. Lett. **134**, 056101 (2025).

[5] Z. Jin, X. Li, and K. Lu, Formation of stable Schwarz crystals in polycrystalline copper at the grain size limit, Phys. Rev. Lett. **127**, 136101 (2021).

[6] H. L. Fu, X. Zhou, Z. P. Gao, Z. H. Jin, X. Y. Li, and K. Lu, Pt Schwarz crystals stabilized by minimal-surface grain boundaries and twins at the grain size limit, Acta Mater. **276**, 120007 (2024).

[7] S. Kasap and P. Capper, *Springer Handbook of Electronic and Photonic Materials* (Springer, Trento, Italy, 2017).

[8] H. B. G. Casimir, Note on the conduction of heat in crystals, Physica **5**, 495 (1938).

[9] P. B. Allen and J. L. Feldman, Thermal conductivity of disordered harmonic solids, Phys. Rev. B **48**, 12581 (1993).

[10] P. B. Allen, J. L. Feldman, J. Fabian, and F. Wooten, Diffusons, locons and propagons: Character of atomic vibrations in amorphous Si, Philos. Mag. B **79**, 1715 (1999).

[11] C. J. Glassbrenner and G. A. Slack, Thermal conductivity of silicon and germanium from 3°K to the melting point, Phys. Rev. **134**, A1058 (1964).

[12] R. O. Pohl, X. Liu, and E. Thompson, Low-temperature thermal conductivity and acoustic attenuation in amorphous solids, Rev. Mod. Phys. **74**, 991 (2002).

[13] H. R. Seyf, L. Yates, T. L. Bougher, S. Graham, B. A. Cola, T. Detchprohm, M.-H. Ji, J. Kim, R. Dupuis, W. Lv, and A. Henry, Rethinking phonons: The issue of disorder, npj Comput. Mater. **3**, 49 (2017).

[14] B. Fultz, C. C. Ahn, E. E. Alp, W. Sturhahn, and T. S. Toellner, Phonons in nanocrystalline ^{57}Fe, Phys. Rev. Lett. **79**, 937 (1997).

[15] H. Frase, B. Fultz, and J. L. Robertson, Phonons in nanocrystalline Ni_3Fe, Phys. Rev. B **57**, 898 (1998).

[16] B. R. Cuenya, L. K. Ono, J. R. Croy, K. Paredis, A. Kara, H. Heinrich, J. Zhao, E. E. Alp, A. T. DelaRiva, A. Datye, E. A. Stach, and W. Keune, Size-dependent evolution of the atomic vibrational density of states and thermodynamic properties of isolated Fe nanoparticles, Phys. Rev. B **86**, 165406 (2012).

[17] J. Kim, H. Kim, M. E. Kilic, C. Gayner, R. Koltun, H. Park, A. Soon, J. Bowers, C. Palmstrøm, and W. Kim, Effect of phonon confinement on the thermal conductivity of $In_{0.53}Ga_{0.47}As$ nanofilms, J. Appl. Phys. **123**, 245103 (2018).

[18] D. Li, Y. Wu, P. Kim, L. Shi, P. Yang, and A. Majumdar, Thermal conductivity of individual silicon nanowires, Appl. Phys. Lett. **83**, 2934 (2003).

[19] M. Tsunoda, T. Honda, K. Ikeda, H. Ohshita, W. Kambara, and T. Otomo, Radial collimator performance and future collimator updates for the high-intensity total scattering diffractometer NOVA at J-PARC, Nucl. Instrum. Methods Phys. Res. Sect. A **1055**, 168484 (2023).

[20] R. Kajimoto *et al.*, The Fermi chopper spectrometer 4SEASONS at J-PARC, J. Phys. Soc. Jpn. **80**, SB025 (2011).

[21] Y. Inamura, T. Nakatani, J. Suzuki, and T. Otomo, Development status of software "Utsusemi" for chopper spectrometers at MLF, J-PARC, J. Phys. Soc. Jpn. **82**, SA031 (2013).

[22] See Supplemental Material at http://link.aps.org/supplemental/10.1103/lqy2-cshl for Tables S1 and S2, and for additional data presented in Figs. S1–S8.

[23] X. Zhao, K. Du, H. Fu, Y. Wang, T. Zheng, C. Hong, X. Li, and K. Lu, Revealing grain boundary plane and curvature of nanostructured metals in three-dimensional space with sub-nanometer resolution, Matter **9**, 102619 (2026).

[24] T. Egami and S. J. L. Billinge, *Underneath the Bragg peaks: Structural Analysis of Complex Materials* (Elsevier, Amsterdam, 2003).

[25] A. S. Masadeh, E. S. Božin, C. L. Farrow, G. Paglia, P. Juhas, S. J. L. Billinge, A. Karkamkar, and M. G. Kanatzidis, Quantitative size-dependent structure and strain determination of CdSe nanoparticles using atomic pair distribution function analysis, Phys. Rev. B **76**, 115413 (2007).

[26] B. Fultz, Vibrational thermodynamics of materials, Prog. Mater. Sci. **55**, 247 (2010).

[27] L. Pasquini, A. Barla, A. I. Chumakov, O. Leupold, R. Rüffer, A. Deriu, and E. Bonetti, Size and oxidation effects on the vibrational properties of nanocrystalline α-Fe, Phys. Rev. B **66**, 073410 (2002).

[28] E. Bonetti, L. Pasquini, E. Sampaolesi, A. Deriu, and G. Cicognani, Vibrational density of states of nanocrystalline iron and nickel, J. Appl. Phys. **88**, 4571 (2000).

[29] B. Fultz, J. L. Robertson, T. A. Stephens, L. J. Nagel, and S. Spooner, Phonon density of states of nanocrystalline Fe prepared by high-energy ball milling, J. Appl. Phys. **79**, 8318 (1996).

[30] C. Dhital, D. L. Abernathy, G. Zhu, Z. Ren, D. Broido, and S. D. Wilson, Inelastic neutron scattering study of phonon density of states in nanostructured $Si_{1-x}Ge_x$ thermoelectrics, Phys. Rev. B **86**, 214303 (2012).

[31] J. Trampenau, K. Bauszus, W. Petry, and U. Herr, Vibrational behaviour of nanocrystalline Ni, Nanostruct. Mater. **6**, 551 (1995).

[32] H. Frase, L. Nagel, J. Robertson, and B. J. P. M. B. Fultz, Vibrational density of states of nanocrystalline Ni_3Fe, Philos. Mag. B **75**, 335 (1997).

[33] R. M. Mazitov, V. A. Semenov, Y. A. Lebedev, R. R. Mulyukov, G. I. Raab, E. L. Yadrovskii, and V. N. Danilenko, Density of phonon states in nanostructured copper, JETP Lett. **92**, 238 (2010).

[34] Y. Shen, C. W. Li, X. Tang, H. L. Smith, and B. Fultz, Phonon anharmonicity and components of the entropy in palladium and platinum, Phys. Rev. B **93**, 214303 (2016).

[35] R. Lübbers, H. F. Grünsteudel, A. I. Chumakov, and G. Wortmann, Density of phonon states in iron at high pressure, Science **287**, 1250 (2000).

[36] A. Zaccone and M. Baggioli, Universal law for the vibrational density of states of liquids, Proc. Natl. Acad. Sci. USA **118**, e2022303118 (2021).

[37] J. B. Suck, H. Rudin, H. J. Guntherodt, H. Beck, J. Daubert, and W. Gläser, Dynamical structure factor and frequency distribution of the metallic glass $Cu_{46}Zr_{54}$ at room temperature, J. Phys. C: Solid State Phys. **13**, L167 (1980).

[38] S. Stankov, Y. Z. Yue, M. Miglierini, B. Sepiol, I. Sergueev, A. I. Chumakov, L. Hu, P. Svec, and R. Rüffer, Vibrational properties of nanograins and interfaces in nanocrystalline materials, Phys. Rev. Lett. **100**, 235503 (2008).

[39] R. Franz and G. Wiedemann, Ueber die Wärme-Leitungsfähigkeit der Metalle, Ann. Phys. **165**, 497 (1853).

[40] R. C. Zeller and R. O. Pohl, Thermal conductivity and specific heat of noncrystalline solids, Phys. Rev. B **4**, 2029 (1971).

[41] A. A. Balandin and D. L. Nika, Phononics in low-dimensional materials, Mater. Today **15**, 266 (2012).

[42] B. Jugdersuren, B. T. Kearney, D. R. Queen, T. H. Metcalf, J. C. Culbertson, C. N. Chervin, R. M. Stroud, W. Nemeth, Q. Wang, and X. Liu, Thermal conductivity of amorphous and nanocrystalline silicon films prepared by hot-wire chemical-vapor deposition, Phys. Rev. B **96**, 014206 (2017).

[43] C. Guthy, C.-Y. Nam, and J. E. Fischer, Unusually low thermal conductivity of gallium nitride nanowires, J. Appl. Phys. **103**, 064319 (2008).

[44] D. Li, Y. Wu, R. Fan, P. Yang, and A. Majumdar, Thermal conductivity of Si/SiGe superlattice nanowires, Appl. Phys. Lett. **83**, 3186 (2003).

[45] J. Hone, M. Whitney, C. Piskoti, and A. Zettl, Thermal conductivity of single-walled carbon nanotubes, Phys. Rev. B **59**, R2514(R) (1999).

[46] T. M. Tritt, *Recent Trends in Thermoelectric Materials Research* (Academic Press, San Diego, CA, 2001).

[47] Z. Wang, R. Xie, C. T. Bui, D. Liu, X. Ni, B. Li, and J. T. L. Thong, Thermal transport in suspended and supported few-layer graphene, Nano Lett. **11**, 113 (2011).

[48] N. Mingo and D. A. Broido, Carbon nanotube ballistic thermal conductance and its limits, Phys. Rev. Lett. **95**, 096105 (2005).

[49] M. Yarali *et al.*, Effects of defects on the temperature-dependent thermal conductivity of suspended monolayer molybdenum disulfide grown by chemical vapor deposition, Adv. Funct. Mater. **27**, 1704357 (2017).

[50] C. Chiritescu, D. G. Cahill, N. Nguyen, D. Johnson, A. Bodapati, P. Keblinski, and P. Zschack, Ultralow thermal conductivity in disordered, layered WSe_2 crystals, Science **315**, 351 (2007).

[51] Z. Wang, J. E. Alaniz, W. Jang, J. E. Garay, and C. Dames, Thermal conductivity of nanocrystalline silicon: Importance of grain size and frequency-dependent mean free paths, Nano Lett. **11**, 2206 (2011).

[52] T. Claudio, G. Schierning, R. Theissmann, H. Wiggers, H. Schober, M. M. Koza, and R. P. Hermann, Effects of impurities on the lattice dynamics of nanocrystalline silicon for thermoelectric application, J. Mater. Sci. **48**, 2836 (2013).

[53] X. Mettan, J. Jaćimović, O. S. Barišić, A. Pisoni, I. Batistić, E. Horváth, S. Brown, L. Rossi, P. Szirmai, B. Farkas, H. Berger, and L. Forró, Tailoring thermal conduction in anatase TiO_2, Commun. Phys. **2**, 123 (2019).

[54] S. Uma, A. D. McConnell, M. Asheghi, K. Kurabayashi, and K. E. Goodson, Temperature-dependent thermal conductivity of undoped polycrystalline silicon layers, Int. J. Thermophys. **22**, 605 (2001).

[55] H. M. Rosenberg, The thermal conductivity of metals at low temperatures, Philos. Trans. R. Soc. London Ser. Math. Phys. Sci. **247**, 441 (1955).

[56] H. N. D. Lang, H. van Kempen, and P. Wyder, The lattice thermal conductivity of very pure aluminium, J. Phys. F: Met. Phys. **8**, L39 (1978).

[57] T. Olsen, Lattice thermal conductivity in copper alloys, J. Phys. Chem. Solids **12**, 167 (1960).

[58] B. R. Cuenya, J. R. Croy, L. K. Ono, A. Naitabdi, H. Heinrich, W. Keune, J. Zhao, W. Sturhahn, E. E. Alp, and M. Hu, Phonon density of states of self-assembled isolated Fe-rich Fe–Pt alloy nanoclusters, Phys. Rev. B **80**, 125412 (2009).

[59] A. I. Hochbaum, R. Chen, R. D. Delgado, W. Liang, E. C. Garnett, M. Najarian, A. Majumdar, and P. Yang, Enhanced thermoelectric performance of rough silicon nanowires, Nature (London) **451**, 163 (2008).

[60] S. Kwon, M. C. Wingert, J. Zheng, J. Xiang, and R. Chen, Thermal transport in Si and Ge nanostructures in the "confinement" regime, Nanoscale **8**, 13155 (2016).

[61] X. Qian, J. Zhou, and G. Chen, Phonon-engineered extreme thermal conductivity materials, Nat. Mater. **20**, 1188 (2021).

[62] B. Golding, B. G. Bagley, and F. S. L. Hsu, Soft transverse phonons in a metallic glass, Phys. Rev. Lett. **29**, 68 (1972).